Electronic Supplementary Information

Quantifying interfacial energetics of 2D semiconductor electrodes using *in situ* spectroelectrochemistry and many-body theory

Rafael Almaraz, Thomas Sayer, Justin Toole, Rachelle Austin, Yusef Farah, Joan M. Redwing, Nicholas Trainor, Amber Krummel, Andrés Montoya-Castillo, and Justin Sambur

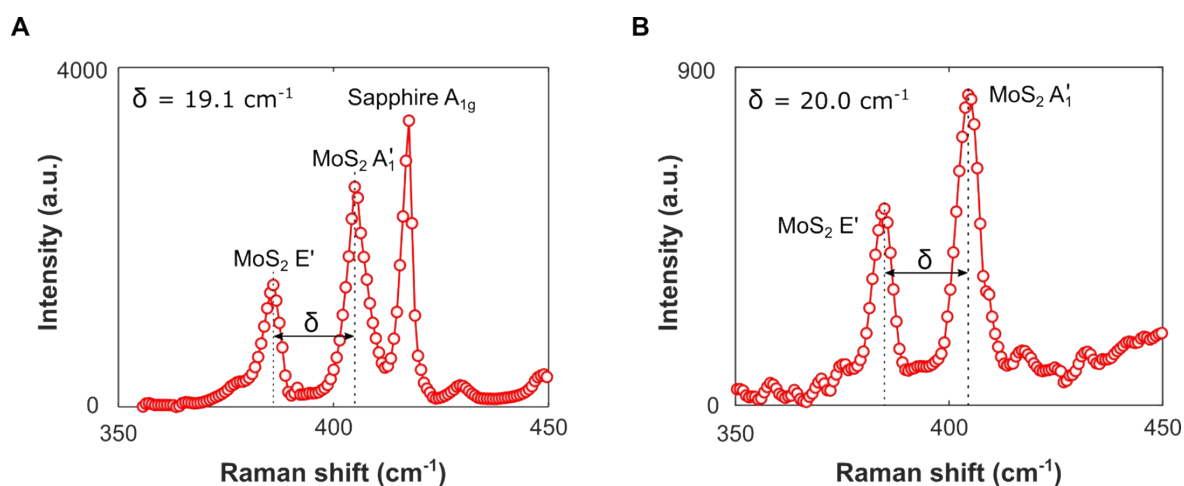Corresponding author: Justin Sambur, Justin.Sambur@colostate.edu

Fig. S1 Representative Raman spectra of MOCVD-synthesized on (A) sapphire and (B) ITO. The Raman peak splitting between the $A_1^{'}$ and $E^{'}$ vibrations is 19.1 cm^{-1} and 20.0 cm^{-1} for the sapphire (as grown) and ITO (transferred) substrates, respectively, in agreement with literature reports for ML-MoS$_2$.[1]. The excitation laser light source is a 532 nm, 1 mW laser. The slight increase in Raman peak splitting is consistent with uniaxial strain from increased surface roughness[2] or additional charge impurities and defects introduced from the transfer to ITO[3] . Note the peak splitting increase did not change to such an extent to indicate multilayer MoS$_2$ (e.g. bi-layer MoS$_2$ peak splitting is 22-23 cm^{-1}).
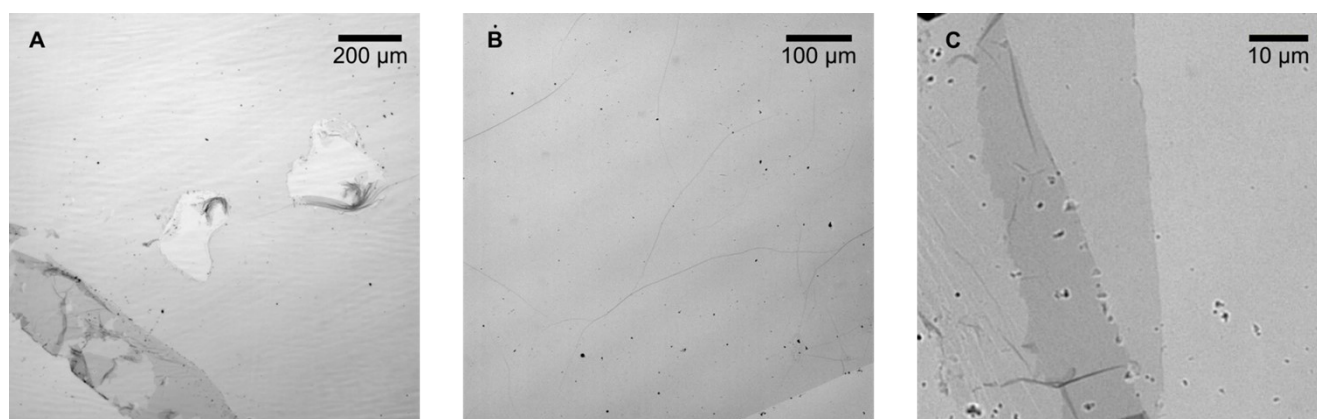

Fig. S2 Representative bright field transmission images of the ML-MoS$_2$ sample in the 3-electrode electrochemical flow cell. **(A)** 10 $\times$ image showing macroscopic defects include two interior tears and a bilayer edge fold. **(B)** 20 $\times$ image showing dark particulate debris and interior micro-folds. **(C)** 60 $\times$ image showing bilayer regions and particulate debris.

Absorbance Error Analysis

Each reported absorbance value in Fig. 2 of the main text is the average of 12-16 hyperspectral images for each incident light wavelength. The uncertainty in absorbance (δA) is determined by propagating the fractional uncertainty in the measurements, $\dfrac{\delta I}{I}$ and $\dfrac{\delta I_0}{I_0}$, using a 95% confidence limit. Assuming $\delta I \geq \delta I_0$, the fractional uncertainty from the logarithmic calculation is $\delta A = 0.434 \times \sqrt{2} \times \dfrac{\delta I}{I}$.[4] The uncertainty is calculated at each spectral step and shown in Fig. S3 below as the shaded region for a single absorbance spectrum. δA is < 0.003 for all reported data and normally < 0.0015 as seen in the inset.
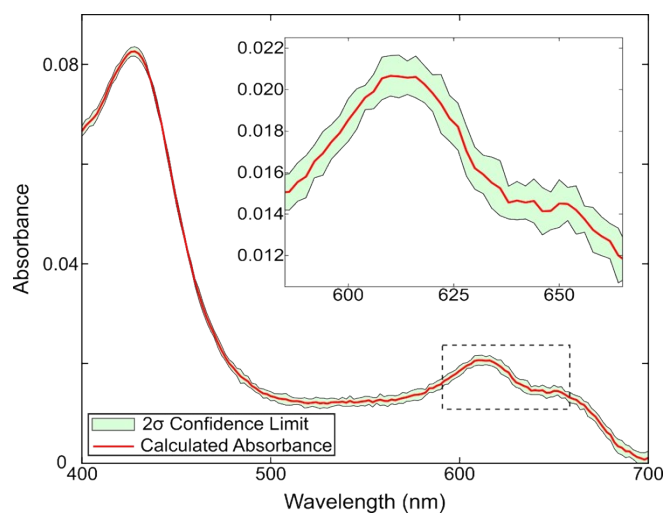
Fig. S3. Representative absorbance spectrum with propagated uncertainty in $A(\lambda)$. The spectrum was collected of ML-MoS$_2$ immersed in electrolyte in an electrochemical cell without an applied potential (V$_{oc}$ = +0.2 V vs Ag). The shaded region represents the 2σ confidence limit for the measurement calculated at each spectral step (i.e., illumination wavelength). The day-to-day variance in absorbance measurements for the same ML-MoS$_2$ sample region was also < 0.003.
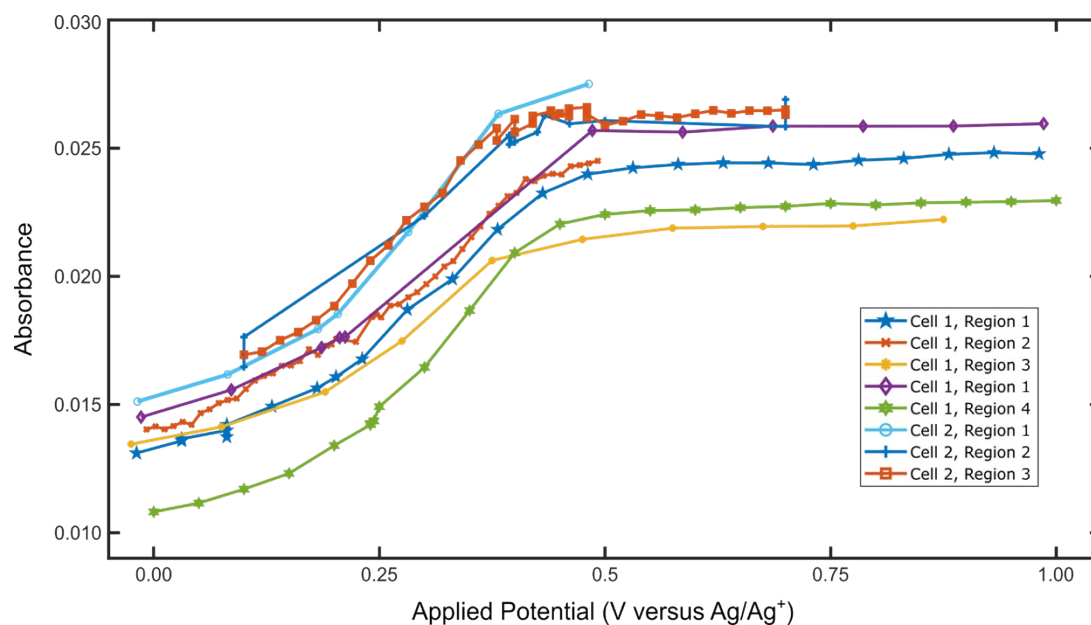

Fig. S4. Absorbance values versus E for multiple ML-MoS$_2$ regions among different electrochemical flow cells. The absorbance values used here are the amplitudes of a Gaussian fit of the A-exciton/trion superpeak.
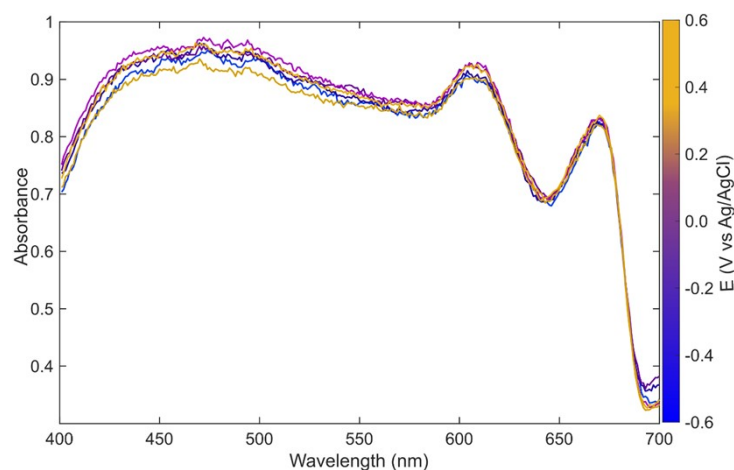
Fig. S5 In situ absorbance data as a function of applied potential for a 50-nm thick (bulk) MoS_2 nanoflake. The A exciton feature shows negligible intensity changes and wavelength shifts changes over a 1.0 V potential range.

Wannier-Mott Model Calculations

The model assumes that the exciton is strongly confined within two dimensions, and that the photogenerated electron in the conduction band and the hole in the valence band have essentially the same magnitude. Therefore, the exciton states are written as a linear combination of the independent electron holes and states and, the carrier density is derived to be[5]:

$$\frac{A_V}{A_0} = \frac{1}{1 + \dfrac{D_n}{D_c}}$$

where A_V is the amplitude from the Gaussian fit at each applied voltage, A_0 is the maximum absorbance, a_0 is the exciton Bohr radius, and D_c is the critical donor density where the exciton is half-bleached ($D_c = 2/\pi a_0^2$). The Bohr radius is influenced by the dielectric environment of the sample and needs to be addressed. The dielectric environment considered here consists of three layers: ε_{ITO}, ε_{MoS_2}, and ε_{MeCN} with reference values for the respective dielectrics taken as 4.0,[6] 12,[7] and 36[8]. The effective dielectric constant, ε_{eff}, is wave vector dependent in ML-MoS_2 because its thickness and exciton radius are comparable. In the large wave vector limit, ε_{eff} approaches ε_{MoS_2} = 12. In the small wave vector limit, ε_{eff} approaches $\dfrac{\varepsilon_{ITO} + \varepsilon_{MeCN}}{2}$ = 21. The dielectric environment, n, and a_0 are not mutually exclusive parameters, so several values of a_0 are used to calculate the carrier
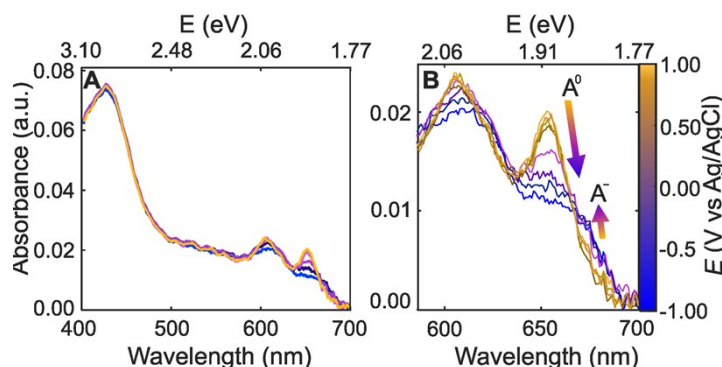
density using the WM model (Fig. S5).[9] The a_0 distances chosen in Fig. S5 correspond to a range of experimental and theoretical results and the ε_{eff} in this study.[7,10,11] Importantly, this shows the dramatic effect of a_0 when using this approach to calculate n from exciton oscillator strength (i.e., relative absorbance values).

Fig. S6 (A) Potential-dependent absorbance spectra of ML-MoS$_2$ in 0.1 M KNO$_3$ aqueous electrolyte. **(B)** ML-MoS$_2$ potential-dependent absorbance highlighting the A-exciton region. The arrows represent potential-dependent absorbance trends for A^0 and A$^-$. The exciton feature diminishes as the trion feature appears, indicating the BGR effect is not limited to non-aqueous electrolytes. Interestingly, the trion absorbance feature appears at E = –0.4 V vs Ag/AgCl in this pH 6 electrolyte, which is more positive than $E^{0'}$(H$^+$/H$_2$) = –0.551 V vs Ag/AgCl. This means trions are likely present in the 2D semiconductor under energy-relevant conditions such as electrocatalytic HER. It is currently unclear to what extent the presence of trions influences the thermodynamics and kinetics of HER, or other fuel-forming reactions, in 2D semiconductors.
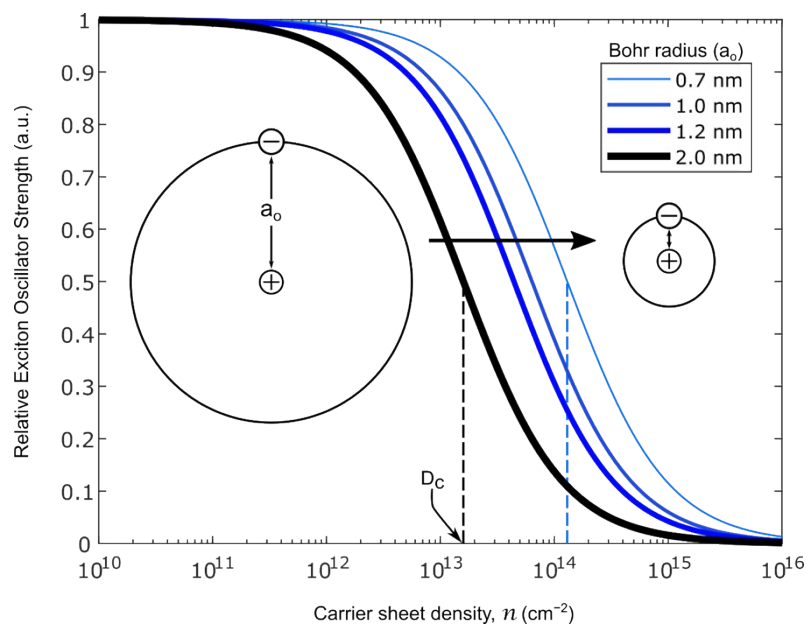

Fig. S7 Relative exciton oscillator strengths as a function of n using the Wannier-Mott model. The critical doping density (D_c) is annotated with a dashed line to highlight the large influence of a_0 on n using this method.
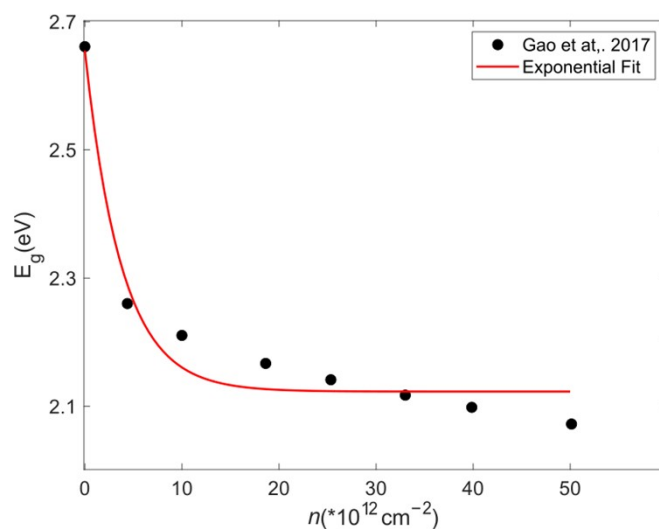

Fig. S8. Electronic bandgap of ML-MoS$_2$ calculated by Gao et. al. (Ref 33 in main text) using a first-principles effective-mass model (black points). The solid red line represents a single exponential fit ($E_g = Ae^{-kn} + y_0$) to the data points, where A = 0.53, k is a decay constant (k = 0.26), and y_0 represents the bandgap at zero doping (y_0 =2.12eV).
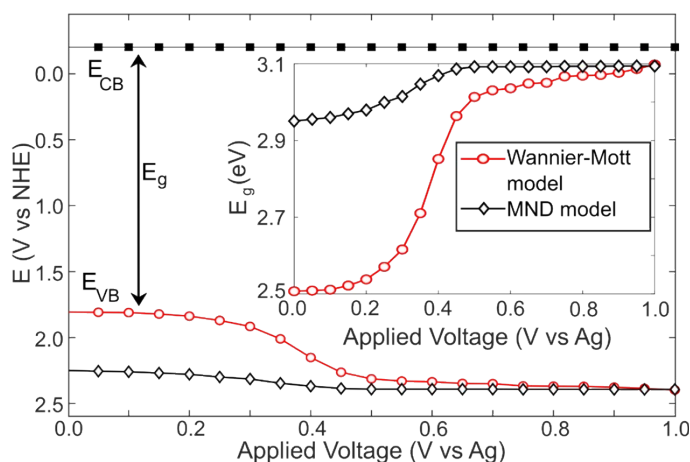
Fig. S9 Additional band energy diagram using E_g values extrapolated from TR-ARPES measurements using the same approach is in Fig. S8, but from data points included in Fig. 4 of ref 17.

Electrochemical Flow Cell Preparation

The custom flow cell preparation is generally detailed in previous work[12]. The typical lateral size of the ML-MoS_2 film ITO was 1-5 mm. The total volume of electrolyte in the cell is 10-80 µL, estimated from the average surface exposed ITO and height of a Teflon spacer. The steady flow of electrolyte reduced potential drift in the Ag wire quasi-reference. Pt (99.9%, Thermo Fisher Sci.) and Ag (99.%, Alfa Aesar) wire served as the working and quasi-reference electrodes, respectively. Both wires were approximately 0.5 mm diameter ✕ 3-4 cm Pt wire (68 µm² surface area). Electrode wires were secured inside the electrolyte reservoir by drilling small holes and applying epoxy (Loctite E-120HP) to create an air-tight seal. The potentiostat applied a constant potential to the ITO/MoS_2 working electrode for the duration of each 5 to 15 min spectral measurement, depending on the full wavelength range shown in Fig. 2 of the main text. The typical open circuit potential was +0.3 V vs Ag/Ag⁺.

Absorbance Measurements

A Horiba OBB Czerny-Turner monochromator (200 mm focal length, 1200 g/mm, 1.2 mm slit) selected 374-700 nm light from a Xe-lamp source and coupled it to the microscope via multi-mode fiberoptics. The bandwidth of emitted light measured against a Horiba iHR550 spectrometer was 4.0 nm (FWHM). A diffusing lens between the fiberoptic line and microscope collimating lens reduced optical aberrations across the 220 x 220 µm image field of view. A 60× 1.2 NA water immersion objective (UPLANSAPO60x/W) collected light passing through the flow cell onto a sensitive CMOS camera (Teledyne Prime 95B). Typically, 150 ms exposure images were collected at 4 frames per second while the monochromator selected each wavelength increment for a duration of 4 or more seconds. To reduce the size of the image datacube, a smaller 200 × 200 pixel (37 × 37 µm) subregion was saved from the full chip 1200 × 1200 pixel (220 × 220 µm). A high-speed data acquisition system (DATAQ DI-4108) recorded the synchronized data from the potentiostat, camera trigger, and monochromator trigger. The hyperspectral image stack was collected using MicroManager software, and raw data was processed offline using MATLAB R2022b.

The monochromatic light transmitted through the system with ML-MoS_2 (I) and "background" light transmitted only through the cell (I_0) were taken as the average intensity of all pixels bound within the respective ROIs of each image (Fig. 1C). Therefore, absorbance is calculated independently for each image, and reported absorbance ($A(\lambda)$) is the average of absorbance values calculated for all (12

-16) respective images within each spectral increment. Importantly, we observed no hysteresis in the potential-dependent absorbance measurements, and the absorbance data reported in the main text was collected using non-sequential applied potentials.

Calculated absorbance varied spatially across a single ML-MoS$_2$ sheet and among different ML-MoS$_2$ sample cells. Regardless of the sample or the number of cycles, we observed the same potential-dependent trends demonstrated in Fig. 2 in the main text. For the 1.0 V potential range, the absolute change in the absorbance peak amplitudes (ΔA) is consistently 0.011 $\pm$ 0.002 (see Fig. S4). The fractional uncertainty of the background intensity $\left(\frac{\delta I_0}{\delta I}\right)$ was spatially invariant, so differences in calculated absorbance likely stem from spatial heterogeneity of the ML-MoS$_2$ material. While outside the scope of this paper, we attribute the spatial variance of the absorbance values to heterogenous domains of varying charge impurities, non-uniform substrate contact (i.e., atomic-scale "wrinkling"), or other defects. Flake-to-flake variation of mechanically exfoliated natural crystals[13,14] and heterogeneity across individual CVD-grown ML-MoS$_2$ flakes[15] has been shown to influence optical measurements. This spatial variation could influence the absolute n value in a minor way, much smaller than the differences shown in Fig. 4 of the main text.

We adopted a Monte Carlo routine to minimize the uncertainty in the absorbance measurement. The routine is not necessary to implement this optical methodology for quantifying interfacial energetics of 2D semiconductor electrodes. The key point of the Monte Carlo analysis is that it indicated the minimum ROI size that reduces the uncertainty in the absorbance measurement by a factor of 5. The ROI size is a subset of random pixels bound within a user-defined region of the transmission image (Fig. 1C). The total size of the ROI boundary is typically 10 – 50 µm in lateral dimensions, corresponding to a total of 15,000 or more pixels. The Monte Carlo routine iterates the absorbance calculation for the same image stack while randomly selecting a defined number of pixels within the ROI (i.e., ROI size). **Fig. S10** shows the influence of ROI size on δA where each square pixel represents 183 nm x 183 nm (0.03 µm^2). Keeping in mind that δA is limited to < 0.003 from the raw "image-to-image" transmission intensity variation, an ROI pixel size of 1000 or more is selected to ensure the ROI sample size does not dominate δA. Noting Fig. S3 and **Fig. S10**, the ML-MoS$_2$ samples are optically homogenous across domains that are tens of micrometers in lateral dimensions. The absorbance spectrum and δA is independently calculated for each iteration. For example, the inset of **Fig. S10**A shows the results of 1,000 Monte Carlo iterations using several different ROI sizes. The A exciton/trion superpeak amplitude and centroid is fit to a Gaussian function for each iteration. A typical Monte Carlo analysis requires less than 1 minute of computational time.
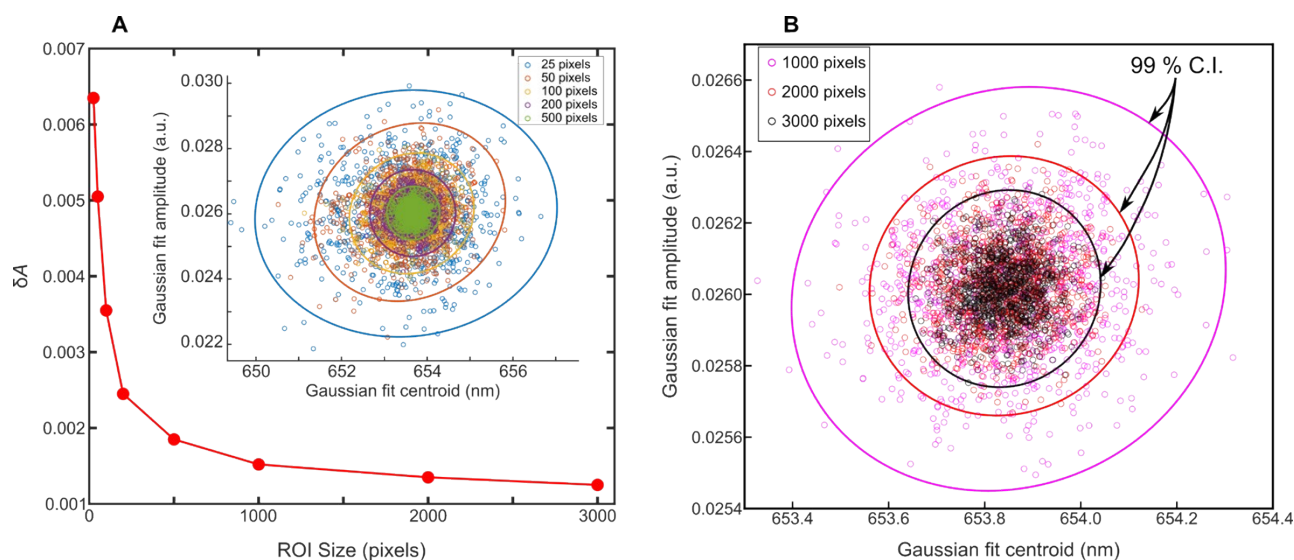

Fig. S10 Monte Carlo results of 1,000 independent absorbance spectra calculations using randomly selected pixels of varying ROI size. (A) Red markers show uncertainty in absorbance (δA) as a function of the number of random pixels selected within the ROI. For each spectrum, the A exciton/trion superpeak is fit to a Gaussian function to extract peak position (centroid) and absorbance (amplitude) parameters. The inset shows a scatter plot of the 1000 best fit parameters for each spectrum using 25 to 500 random pixels; (B) Ellipses denote the 99 % confidence intervals (C.I.) in the absorbance peak Gaussian fit parameters for the three largest effective ROI sizes. The range of peak amplitude fits (i.e., absorbance) is consistently < 0.002 for ROIs comprised of 1,000 or more pixels. The random pixels are selected from a user-defined ROI region that is > 15,000 pixels.

Material Characterization

Confocal Raman micro-spectroscopy was performed on an Olympus IX-73 optical microscope with a 532 nm Ondax THz laser source. Incident light focused on the sample through a 100 $\times$ NA 0.95 air objective (Olympus PlanFL N100X) with a beam diameter of 0.7 μm (determined from FWHM of the beam profile). The laser power at the sample was typically 1 mW. Light was collected in a backscattering geometry, filtered by the Ondax system, passed through a Horiba iHR550 imaging spectrometer (1800 and 1200 gr/mm), and detected on a Synapse back-illuminated deep depletion charge-coupled device (CCD). The Raman spectra are the average of four sequential 30 s acquisitions. The spectral resolution is < 1 cm^{-1}. The system was calibrated to the pair of Stokes and anti-Stokes Raman peaks for either crystalline silicon ($\pm$ 520.8 cm^{-1}) or sapphire A$_{1g}$ ($\pm$ 417.4 cm^{-1}). All measurements occurred in air at room temperature.

5-step procedure to determine best ε_F value for every *E*

In step 1, we convolve the MND model with the broadening Gaussian to calculate a set of absorbance spectra as a function of ε_F. In Step 2, we perform a linear background subtraction for each experimental spectrum in Fig. 2 and calculate the absolute error between the background-corrected experimental spectrum and all simulated curves in Step 1. The sum of the best-fit errors from the 'global' set defines a total error. In Step 3, we make a small change to the height, width, and positions of the A^0 and A$^-$ peaks as a function of potential, subject to the constraints established by the MND model, and repeat Steps 1–2. In Step 4, we accept the parameter changes from Step 3 if it lowers the total error. We reject the changes in Step 3 if the total error is not lowered by using the Metropolis Monte Carlo method with an effective temperature chosen to allow a few percent of steps when at a local minimum. In Step 5, we iterate Steps 1-4 until the error satisfactorily converges; in all cases we achieve qualitatively good agreement between experiment and theory. More robust details are found in our previous work (Reference 37) from the main text).

Calibrating the QRE versus a commercial non-aqueous fritted Ag/AgNO$_3$ electrode

We acquired all electrochemical and optical data versus an Ag wire quasi reference electrode (QRE). We calibrated the actual potential of this QRE versus a calibrated, commercial reference electrode (Ag/AgNO$_3$ electrode, CHI #112, 3 mm). To do so, we measured cyclic voltammograms (CVs) of ferrocene/ferrocenium (Fc/Fc$^+$) using polished Pt disc working and counter electrodes (CHI #102, 3 mm), and either the Ag wire QRE or the commercial Ag/AgNO$_3$ electrode. Fig. S11 shows CVs of 1 mM Fc/Fc$^+$ in dry, air-free 0.25 M NBu$_4$PF$_6$ acetonitrile electrolyte against both reference electrodes. The peak splitting (ΔE_p) is 68 mV for both reference electrodes. Next, we calculated $E^{0'}$ values from $E_{1/2}$ values, $0.5(E_{p,a} + E_{p,c})$, where $E_{p,a}$ and $E_{p,c}$ are the anodic and cathodic peak potentials. Here we assumed differences in the diffusion coefficients of the oxidized and reduced species are negligible ($D_{Fc} \cong D_{Fc^+}$).[16] The $E^{0'}_{Fc/Fc^+}$ values versus the 0.01 M Ag/AgNO$_3$ reference electrode is +0.056 V, which agrees with literature.[17,18] The $E^{\circ'}_{Fc/Fc^+}$ values versus the Ag/Ag$^+$ QRE is +0.106 V. Thus, the potential of our Ag QRE to the standard Ag/AgNO$_3$ reference is −0.050 V (Eqn. S1 below). The potential of the Ag/AgNO$_3$ reference to the NHE scale is $+$0.548 V (Eqn. S2).[19] Finally, we sum (Eqn. S1) and (Eqn. S2) to yield the potential of our Ag wire QRE to NHE scale (Eqn. S3). The potential of our QRE did not drift more than 5 mV over several months, as evidenced by repeat open circuit potentials.

$$E \text{ (V vs 0.01 M AgNO}_3 \text{ / Ag)} = E \text{ (V vs Ag QRE)} - 0.050 \text{ V} \qquad \text{(Eqn. S1)}$$

$$E \text{ (V vs NHE)} = E \text{ (V vs 0.01 M AgNO}_3 \text{ / Ag)} + 0.548 \text{ V} \qquad \text{(Eqn. S2)}$$

$$E \text{ (V vs Ag QRE)} = E \text{ (V vs NHE)} - 0.498 \text{ V} \qquad \text{(Eqn. S3)}$$
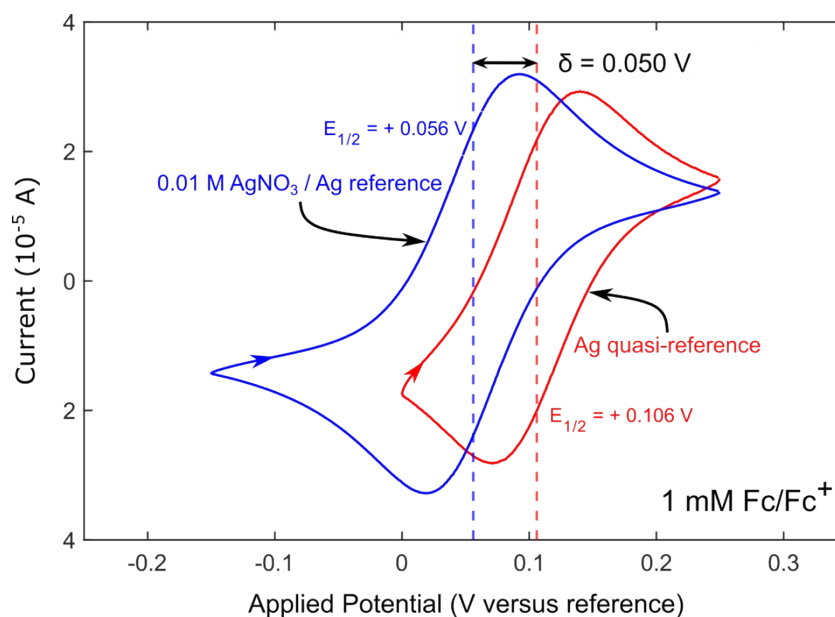
Fig. S11 Cyclic voltammograms of 1 mM ferrocene/ferrocenium in dry 0.25 M NBu_4PF_6 acetonitrile vs either an Ag wire QRE (red trace, right) and standard non-aqueous $Ag/AgNO_3$ fritted reference (blue trace, left). The scan rate is 100 mV/s. The working and counter electrodes were polished Pt discs with geometric surface areas of 0.07 cm^2.

References

1   C. Lee, H. Yan, L. E. Brus, T. F. Heinz, J. Hone and S. Ryu, *ACS Nano*, 2010, **4**, 2695–2700.
2   A. Castellanos-Gomez, R. Roldán, E. Cappelluti, M. Buscema, F. Guinea, H. S. J. van der Zant and G. A. Steele, *Nano Lett.*, 2013, **13**, 5361–5366.
3   S. Mignuzzi, A. J. Pollard, N. Bonini, B. Brennan, I. S. Gilmore, M. A. Pimenta, D. Richards and D. Roy, *Phys. Rev. B*, 2015, **91**, 195411.
4   J. Taylor, *Introduction to error analysis, the study of uncertainties in physical measurements*, University Science Books, 1997.
5   G. M. Carroll, H. Zhang, J. R. Dunklin, E. M. Miller, N. R. Neale and J. van de Lagemaat, *Energy Env. Sci*, 2019, **140**, 441–9.
6   C.-W. Chen, Y.-C. Lin, C.-H. Chang, P. Yu, J.-M. Shieh and C.-L. Pan, *IEEE J. Quantum Electron.*, 2010, **46**, 1746–1754.
7   C. Zhang, H. Wang, W. Chan, C. Manolatou and F. Rana, *Phys. Rev. B*, 2014, **89**, 205436.
8   I. N. Daniels, Z. Wang and B. B. Laird, *J. Phys. Chem. C*, 2017, **121**, 1025–1031.
9   D. Huang, J.-I. Chyi and H. Morkoç, *Phys. Rev. B*, 1990, **42**, 5147–5153.
10 T. Cheiwchanchamnangij and W. R. L. Lambrecht, *Phys. Rev. B*, 2012, **85**, 205302.
11 X. Zhu, N. R. Monahan, Z. Gong, H. Zhu, K. W. Williams and C. A. Nelson, *J. Am. Chem. Soc.*, 2015, **137**, 8313–8320.
12 L. Wang and J. B. Sambur, *Nano Lett.*, 2019, **19**, 2960–2967.
13 S. McDonnell, R. Addou, C. Buie, R. M. Wallace and C. L. Hinkle, *ACS Nano*, 2014, **8**, 2880–2888.
14 Y. Niu, S. Gonzalez-Abad, R. Frisenda, P. Marauhn, M. Drüppel, P. Gant, R. Schmidt, N. Taghavi, D. Barcons, A. Molina-Mendoza, S. de Vasconcellos, R. Bratschitsch, D. Perez de Lara, M. Rohlfing and A. Castellanos-Gomez, *Nanomaterials*, 2018, **8**, 725–28.
15 K. Yao, A. Yan, S. Kahn, A. Suslu, Y. Liang, E. S. Barnard, S. Tongay, A. Zettl, N. J. Borys and P. J. Schuck, *Phys. Rev. Lett.*, 2017, **119**, 087401–6.
16 Y. Wang, E. Rogers and R. Compton, *J. Electroanal. Chem.*, 2010, **648**, 15–19.

17 J. A. Baglio, G. S. Calabrese, D. J. Harrison, E. Kamieniecki, A. J. Ricco, M. S. Wrighton and G. D. Zoski, *J. Am. Chem. Soc.*, 1983, **105**, 2246–2256.

18 N. G. Tsierkezos and U. Ritter, *J. Appl. Electrochem.*, 2010, **40**, 409–417.

19 V. V. Pavlishchuk and A. W. Addison, *Inorganica Chim. Acta*, 2000, **298**, 97–102.